

Formation of correlated chromatin domains at nanoscale dynamic resolution during transcription

Haitham A. Shaban^{1,2,*}, Roman Barth^{1,†} and Kerstin Bystricky^{1,*}

¹Laboratoire de Biologie Moléculaire Eucaryote (LBME), Centre de Biologie Intégrative (CBI), CNRS, University of Toulouse, UPS, 31062 Toulouse, France and ²Spectroscopy Department, Physics Division, National Research Centre, Dokki, Cairo, Egypt

Received January 04, 2018; Revised February 15, 2018; Editorial Decision March 24, 2018; Accepted April 03, 2018

ABSTRACT

Intrinsic dynamics of chromatin contribute to gene regulation. How chromatin mobility responds to genomic processes, and whether this response relies on coordinated chromatin movement is still unclear. Here, we introduce an approach called Dense Flow reConstruction and Correlation (DFCC), to quantify correlation of chromatin motion with sub-pixel sensitivity at the level of the whole nucleus. DFCC reconstructs dense global flow fields of fluorescent images acquired in real-time. We applied our approach to analyze stochastic movements of DNA and histones, based on direction and magnitude at different time lags in human cells. We observe long-range correlations extending over several μm between coherently moving regions over the entire nucleus. Spatial correlation of global chromatin dynamics was reduced by inhibiting elongation by RNA polymerase II, and abolished in quiescent cells. Furthermore, quantification of spatial smoothness over time intervals up to 30 s points to clear-cut boundaries between distinct regions, while smooth transitions in small ($<1 \mu\text{m}$) neighborhoods dominate for short time intervals. Rough transitions between regions of coherent motion indicate directed squeezing or stretching of chromatin boundaries, suggestive of changes in local concentrations of actors regulating gene expression. The DFCC approach hence allows characterizing stochastically forming domains of nuclear activity.

INTRODUCTION

Nuclear organization is characterized by short- and long-range contacts, bringing chromosome domains into spatial proximity and creating chromosome territories (CT) de-

tectable by fluorescent *in situ* hybridization (1,2) and high-throughput chromosome conformation capture (Hi-C) (3) in human cells. Live cell imaging of CTs identified random and directed motion of sub-chromosomal foci, and suggested similarities in dynamic behavior between distinct CTs (4). On the time scale of several seconds, chromatin was shown to move coherently irrespective of CT boundaries, suggestive of transient mechanical coupling of chromatin over a few microns (5,6). Fluctuations in chromatin architecture also occur over a large range of spatio-temporal scales during DNA transcription, and repair (6–8). This range of variations makes studying molecular organization and dynamic processes of the whole genome challenging. In particular, gene transcription depends on chromatin dynamics to fine-tune expression levels (9). Active genes sometimes gather dynamically to share the same transcription sites (10–12), and the range of coordinated chromatin movement is thought to correlate with mRNA production and enhancer activity (10). Coordinated relocalization or extrusion of activated genes to the surface of CTs is coherent with the idea that this process favors reaching shared transcription factors (13–16). The mechanism of such movements is unknown.

Chromatin motion during processes related to genome function in mammalian cells can be studied by fluorescence live imaging. Most of these studies rely on labeling single loci or arrays of repeated DNA sequences with assistance of gene editing techniques (17–22). Single particle tracking demonstrated that motion of the tagged DNA loci is sub-diffusive although super-diffusive behavior was reported (20,21). In particular, motion of telomeres is particularly heterogeneous (23–25). Large fluctuations in sub-diffusive behavior were also determined for H2B-GFP imaged with sub-second time intervals (26,27). To gain a true understanding of the physical nature of a long fiber structure such as genomic chromatin, chromatin has to be analyzed at a large scale across the entire nucleus. Recently, an analysis based on correlation spectroscopy of time-resolved imag-

*To whom correspondence should be addressed. Tel: +33 561 335 860; Fax: +33 561 335 886; Email: haitham.shaban@ibcg.biotoul.fr
Correspondence may also be addressed to Kerstin Bystricky. Tel: +33 561 335 831; Fax: +33 561 335 886; Email: kerstin.bystricky@ibcg.biotoul.fr

†The authors wish it to be known that, in their opinion, the first two authors should be regarded as Joint First Authors.

Present address: Roman Barth, Faculty of Applied Sciences, Delft University of Technology, 2628 CJ Delft; The Netherlands.

ing using particle imaging velocimetry (PIV) (6) presented a global view of chromatin dynamics. However, in this study, a relatively large interrogation window size of more than one micrometer was set to estimate the displacement vectors for PIV. Dynamic changes within the set window cannot be assessed by this approach, leaving the contribution of genomic processes to local chromatin motion, typically taking place at the nanometer scale, undisclosed.

Here, we introduce a method called Dense Flow reConstruction and Correlation (DFCC) to quantify the correlation of chromatin motion with sub-pixel sensitivity at the level of the whole nucleus. DFCC provides sub-diffraction vectorial information, based on reconstructed dense global flow fields of a series of diffraction limited fluorescent images. The sample pixel size defines the dynamic resolution of the results independently of its dimensions (here down to 65 nm). We use optical flow (OF) to estimate the direction and amplitude of the motion of fluorescent labeled DNA and histones over a 30 s time interval at five frames per second (fps), and confirm that this OF formulation is more sensitive than PIV for studying the motion of intracellular objects (28). We calculate the spatial and temporal correlation of motion from both direction and amplitude of each displacement vector, and quantify characteristic length scales of correlated motion with nano-scale resolution. Estimation of the smoothness of flow fields across the whole nucleus at different transcriptional stages reveals coherently moving chromatin domains.

MATERIALS AND METHODS

Cell culture. A stable human osteosarcoma U2OS cell line (ATCC) stably expressing H2B-GFP was a gift from Sébastien Huet (Rennes, France). Cells were grown in Dulbecco's modified Eagle's medium (DMEM) containing phenol red-free (Sigma-Aldrich) supplemented with 10% fetal bovine serum (FBS), Glutamax containing 50 μ g/ml gentamicin (Sigma-Aldrich), 1 mM sodium pyruvate (Sigma-Aldrich) and G418 0.5 mg/ml (Sigma-Aldrich) at 37°C with 5% CO₂. Cells were plated for 24 h on 35 mm petri dishes with a #1.5 coverslip like bottom (μ -Dish, Ibidi, Biovalley) with a density of 10⁵ cells/dish.

DNA staining. For DNA staining, the same cell line of U2OS was labeled by using SiR-DNA (SiR-Hoechst) kit (Spirochrome AG). SiR-DNA is a far-red fluorophore that binds to the DNA minor groove with high specificity (29). Briefly, 1 mM stock solution was prepared by dissolving the content of the vial of SiR-DNA in 50 μ l of anhydrous Dimethyl sulfoxide (DMSO). This solution should be stored at -20°C. For labeling, we diluted the stock solution in cell culture medium to concentration of 2 μ M and vortexed briefly. On the day of the imaging, the culture medium was changed to medium containing SiR-fluorophores and incubated at 37°C for 30–60 min. Before imaging, the medium was replaced by L-15 medium (Liebovitz's, Gibco). Cells were mounted on the microscope for live imaging in a custom-built 37°C microscope incubator.

Cell starvation, stimulation and chemical treatment

Transcription inhibition and stimulation. For cell starvation, the media were replaced with serum-free medium (DMEM, Glutamax containing 50 μ g/ml gentamicin, 1 mM sodium pyruvate, and G418 0.5 mg/ml). Cells were incubated for 24 h in the 37°C incubator before imaging. Just before imaging, the medium was changed to L-15 medium. Cell starvation conditions were used for transcription inhibition mode. While for stimulation mode, cells were incubated with full medium containing 10% FBS, and imaged with 10% FBS in L-15 medium.

Transcription blocking. To assess the impact of transcription initiation on chromatin motion in living cells, we added fresh L-15 medium containing 1 μ M triptolide (TPL, Sigma-Aldrich). To block transcription elongation, 100 μ M of 5,6-dichloro-1- β -D-ribofuranosylbenzimidazole (DRB, Sigma-Aldrich) was diluted in fresh L-15 medium and incubated under the microscope for 15 min before imaging.

Microscopy and image acquisition

SiR-Hoechst labeled DNA imaging. DNA images were acquired using a DMI8 inverted automated microscope (Leica Microsystems) featuring a confocal spinning disk unit (CSU-X1-M1N, Yokogawa). Integrated laser engine (ILE 400, Andor) with a selected wavelength of 647 nm (140 mW) was used for excitation. Samples were imaged with an oil immersion objective (Leica HCX-PL-APO 100x/1.4 NA). Fluorescence emission of the SiR-Hoechst was filtered by a single-band bandpass filter (FF01-650/13-25, Semrock, Inc.). Image series of 150 frames (5 fps) were acquired using Metamorph software (Molecular Devices), and detected using sCMOS cameras (ORCA-Flash4.0 V2) and (1 \times 1 binning), with sample pixel size of 65 nm. All series were recorded at 37°C and in a humid chamber by controlling the temperature and CO₂ control flow using H201—couple with temperature and CO₂ units.

H2B-GFP imaging. Series of 150 frames were acquired with an exposure time of 200 ms using a Nipkow-disk confocal system (Revolution, Andor) featuring a confocal spinning disk unit (CSU22, Yokogawa). A diode-pumped solid-state laser with a single laser line was used for excitation of GFP at 488 nm (25 mW; Coherent). Samples were imaged with an oil immersion objective (100 \times , Plan Apo 1.42, Nikon) followed by 2 \times magnification and fluorescence was filtered with an emission filter (ET525/30-25, Semrock, Inc.). The fluorescent emission was detected on a cooled electron multiplying charge-coupled device camera (iXon Ultra 888), with sample pixel size of 88 nm. The system was controlled using the Revolution IQ software (Andor).

Methods evaluation

Simulation of microscopic and dynamic parameters for quantitative chromatin imaging. In order to evaluate the accuracy of different OF methods quantitatively for chromatin motion, ground truth data is required, but unavailable for biological systems. To overcome this lack we simulated images recapitulating our experimental conditions with a

range of microscopic (labeling density, Signal-to-Noise ratio (SNR)) and dynamic (diffusion coefficient, number of independently moving domains) parameters. In this study, we considered five OF methods that cover four types of OF, namely differential methods (Horn–Schunck (HS); Lucas–Kanade (LK) formulations) (30,31), region-based matching (hereafter Particle Image Velocimetry—PIV) (32), phase-based methods (33) and SIFT-based methods (34). Details of all the tested algorithms can be found in Supplementary Note 1. We evaluated the performance of the different methods by determining the angular error (AE) and the endpoint error (EE) in simulated datasets. The simulation of data samples was carried out by randomly placing emitters with a defined density in a given volume with varying SNR as described in (Supplementary Note 1 and Supplementary Figure S1). A series of two images was simulated where emitters undergo Brownian diffusion and therefore are displaced from one image to another. We simulated a density ranging from 0.02 to 2.5 emitters per pixel representing the spatial variation of chromatin compactness within hetero- and euchromatin (26) (Supplementary Figure S1a–c). Further, we varied the particles' diffusion coefficient as well as the number of coherently moving domains which could potentially reflect chromatin motion at different length scales (Supplementary Figure S1f and g). The images were then subjected to OF algorithms in order to reconstruct the direction and magnitude of the emitters' movements. Regions within the emitters are forced to undergo coherent motion were superimposed as described in (Supplementary Note 1).

Quantitative evaluation. A vector is determined by its direction and magnitude. The AE and EE are common measures used for performance evaluation of flow estimation methods. The AE is the angle between the ground-truth vector $\vec{V} = (u, v)$ and the corresponding estimated vector $\vec{V}' = (u', v')$ and is computed as the inverse cosine of the normalized dot-product of $\vec{V} = (u, v)$ and $\vec{V}' = (u', v')$ (35):

$$AE = \cos^{-1} \left(\frac{\vec{V} \cdot \vec{V}'}{|\vec{V}| |\vec{V}'|} \right).$$

As an angle between an arbitrary vector and the zero vector is not defined, we only take non-zero displacements into consideration.

The AE is a relative measure and penalizes discrepancies in the direction of ground-truth and estimated flow. The evaluation of errors in the magnitude is given by the absolute EE (36).

$$EE = |\vec{V} - \vec{V}'|.$$

All calculations were carried out using MATLAB (MATLAB Release 2017a, The MathWorks, Inc., Natick, MA, USA) on a 64-bit Intel Xeon CPU E5-2609 1.90 GHz workstation with 64 GB RAM and running Microsoft Windows 10 Professional.

Image processing and data analysis

Denoising. Raw images were denoised using non-iterative bilateral filtering (37). While Gaussian blurring only accounts for the spatial distance of a pixel and its neighborhood, bilateral filtering additionally takes the difference in intensity values into account and is therefore an edge-preserving method. Abrupt transitions from high- to low-intensity regions (e.g. heterochromatin to euchromatin) are not over-smoothed.

Drift registration. Drift during image acquisition was determined by the cross correlation of the first image in the sequence and every following image of the whole nucleus. The position of the correlation peak is found with sub-pixel accuracy by a Gaussian approximation of the correlation peak. The distance of the correlation peak from the origin is the desired drift vector. The detected drift in all processed image sequences was in the range of <10 nm and is therefore negligible.

Spatial correlation calculation. The spatial auto-correlation function r of a scalar field $\gamma(x, y)$ can be calculated efficiently by the use of Fast Fourier Transform algorithms and is given by (38):

$$r(\Delta x, \Delta y) = \frac{\mathcal{F}^{-1}[\mathcal{F}(\gamma) \cdot \mathcal{F}^*(\gamma)]}{\gamma\gamma},$$

where $\mathcal{F}(\cdot)$, $\mathcal{F}^{-1}(\cdot)$, and $\mathcal{F}^*(\cdot)$ are the Fourier transformation, inverse Fourier transformation and the complex conjugate of the Fourier transformation, respectively. The two-dimensional (2D) auto-correlation function was calculated for horizontal and vertical space lag as denoted by $r(\Delta x, \Delta y)$. One can project the 2D correlation function onto one dimension using the space lag $\rho^2 = \Delta x^2 + \Delta y^2$. The projection was carried out as a radial average and the correlation function becomes a function of the space lag only, i.e. $r = r(\rho)$.

Correlation modeling of dense motion fields. Vector fields produced by OF algorithms may be considered as two independent scalar fields representing direction and magnitude of the vector field. Each value in these fields can be described as a stochastic variable which led us to consider the scalar fields as random fields. This allows parametrization of the correlation of chromatin dynamics in each random field using the Whittle–Matérn (WM) model (39,40):

$$r(\rho) = \frac{2^{1-\nu}}{\Gamma(\nu)} \left(\frac{\rho}{\rho_c} \right)^\nu K_\nu \left(\frac{\rho}{\rho_c} \right).$$

Where, $\Gamma(\cdot)$ is the gamma function; $K_\nu(\cdot)$ is the modified Bessel function of the second type of order ν , ρ_c is the correlation length and ν is a smoothness parameter (Supplementary Note 2). The WM model has important advantages for modeling spatial processes by including a parameter which characterizes the smoothness of the corresponding random fields. Large ν means that the underlying spatial process is smooth in space, whereas the process is considered as rough for small ν (41,42) (Supplementary Note 2; Supplementary Figures S3 and 4). An analogy between the smoothness of

a random field and its differentiability can be drawn (provided $\nu \geq 1$) (43). The association of the smoothness parameter to the existence of directional derivatives gives rise to the concept that a smooth field does not exhibit singular points and is continuous in the domain of computation. Smooth fields are uncommon for natural processes, but the parametrization of smoothness allows identifying sharp transitions (e.g. object boundaries, singular points) in a quantified manner.

RESULTS AND DISCUSSION

Comparison of optical flow methods for precise estimation of chromatin dynamics by simulations

OF methods estimate the 2D apparent motion field of two consecutive images in an image sequence, and enable assigning a displacement vector to each pixel. In this study, we considered five OF methods described above, namely differential HS and LK formulations (30,31), region-based matching (PIV) (32), phase-based (33) and SIFT-based methods (34). AE and EE are common measures to evaluate the accuracy of motion estimation techniques in both direction and magnitude of these methods, respectively. First we tested the impact of labeling density on the accuracy of the methods to define vectors AE and EE. We noticed that by increasing labeling density, error measures increased for all methods. A jump was seen in the EE of the HS formulation once the density approaches $\sim 1/px$. Although HS and PIV (window size 16×16 pixels) performed best, HS had the lowest AE ($<10^\circ$), 2-fold better than PIV (16×16 pixels).

Next, we considered variations in SNR due to characteristics of the specimen and intrinsic signal-dependent Poisson noise (Supplementary Figure S1d and e). Figure 1 shows that the accuracy of all methods decreases with noise and a characteristic step at $\text{SNR} \approx 90$ can be observed. The EEs of PIV methods using a small window size (8×8 pixels or smaller) were particularly sensitive to low SNR because PIV methods calculate the displacement vector based on the peak position of the correlation peak. At high SNR noise peaks become dominant and the probability to select an erroneous peak increases (44), and therefore small displacements tend to disproportionately increase the EE.

OF methods should be sensitive to displacement magnitude in order to capture the temporal and spatial amplitude of chromatin dynamics, typically characterized by diffusion coefficients at single genes and telomeres ranging from $10^{-3} \mu\text{m}^2/\text{s}$ to $10^{-4} \mu\text{m}^2/\text{s}$ (6,23,24,26,45). Increasing the emitters' diffusion coefficient, i.e. increasing the distance by which each emitter is allowed to move per time step, enhanced the accuracy in determining the direction of displacement. OF methods using coarse-to-fine estimation schemes (iterative refinement of flow fields on subsampled versions of the input images, see Supplementary Note 1) did not show substantially different trends than methods without a pyramidal structure (Figure 1).

Varying the number of independently moving domains showed that errors increased with greater complexity in motion independently of the method employed. For 10 domains and more, the LK-based method outperformed the

HS formulation in terms of AE. Nevertheless, if the accuracy of the method is assessed by EE, the HS method performed substantially better than all other methods.

Several PIV methods differing by their interrogation window size were tested. The accuracy achieved by these methods was dependent on the window size. Although the AE of PIV using a window size of 16×16 pixels was as low as the AE of the HS method, PIV failed to identify different domains of coherent motion. Based on our simulations, we determined that the interrogation window size used in PIV should be equal or larger than the expected maximal displacement. Otherwise, emitters moving out of the interrogation window create errors resulting from calculations of cross-correlation from signal loss. Therefore, the window-size must be carefully adjusted to the data. Multiple small independently moving objects within the same sub-region might lead to erroneous results due to several independent motions within the pattern. Careful adjustment of the window size is particularly difficult when studying chromatin dynamics (6), where the expected density of emitters and their dynamic behavior is hard to predict.

On average, the HS-based method outperformed all other methods and was thus chosen as the most reliable for the experimental analysis hereafter. In conclusion, our simulations show that the HS based OF method is appropriate for studying chromatin dynamics based on fluorescence imaging.

Dense flow correlation of chromatin dynamics based on real time imaging in 2D

We determined flow fields of chromatin motion based on real time imaging (a series of 150 single plane images acquired at 5 fps) of a single U2OS nucleus expressing H2B-GFP (Figure 2A and B) and compared the response of the five methods under consideration. The empirical correlation was calculated and projected onto the one-dimensional space lag ρ from two successive representative images (see 'Materials and Methods' section, Figure 2C and D). We applied the WM model to extract the correlation length, which represents the typical length scale over which the correlation of two vectors diminishes (for both direction and magnitude), and the smoothness parameter, which quantifies the sharpness of transitions, i.e. the rate of change in direction or magnitude across a distance and the amount of singular points (e.g. vortices) in the region of interest (Supplementary Note 2). Figure 3 shows the mapped direction and magnitude of each single vector across a single entire nucleus (Figure 3A and B). In the flow field of the LK method, one could hardly observe large regions of coherent motion, neither in direction nor in magnitude. The flow field was rough, showing many small areas and therefore correlation dropped right after the zero space lag (Figure 3C). This behavior was seen in both direction and magnitude. Consistent with our simulations, the window size of PIV methods influenced their ability to distinguish between regions of coherent flow. PIV with a 16×16 pixel window size showed numerous small regions of coherent motion (in direction only) but did not permit a clear distinction between direction and magnitude of spatial correlations. Moreover, correlation dropped sharply after the zero space lag for both

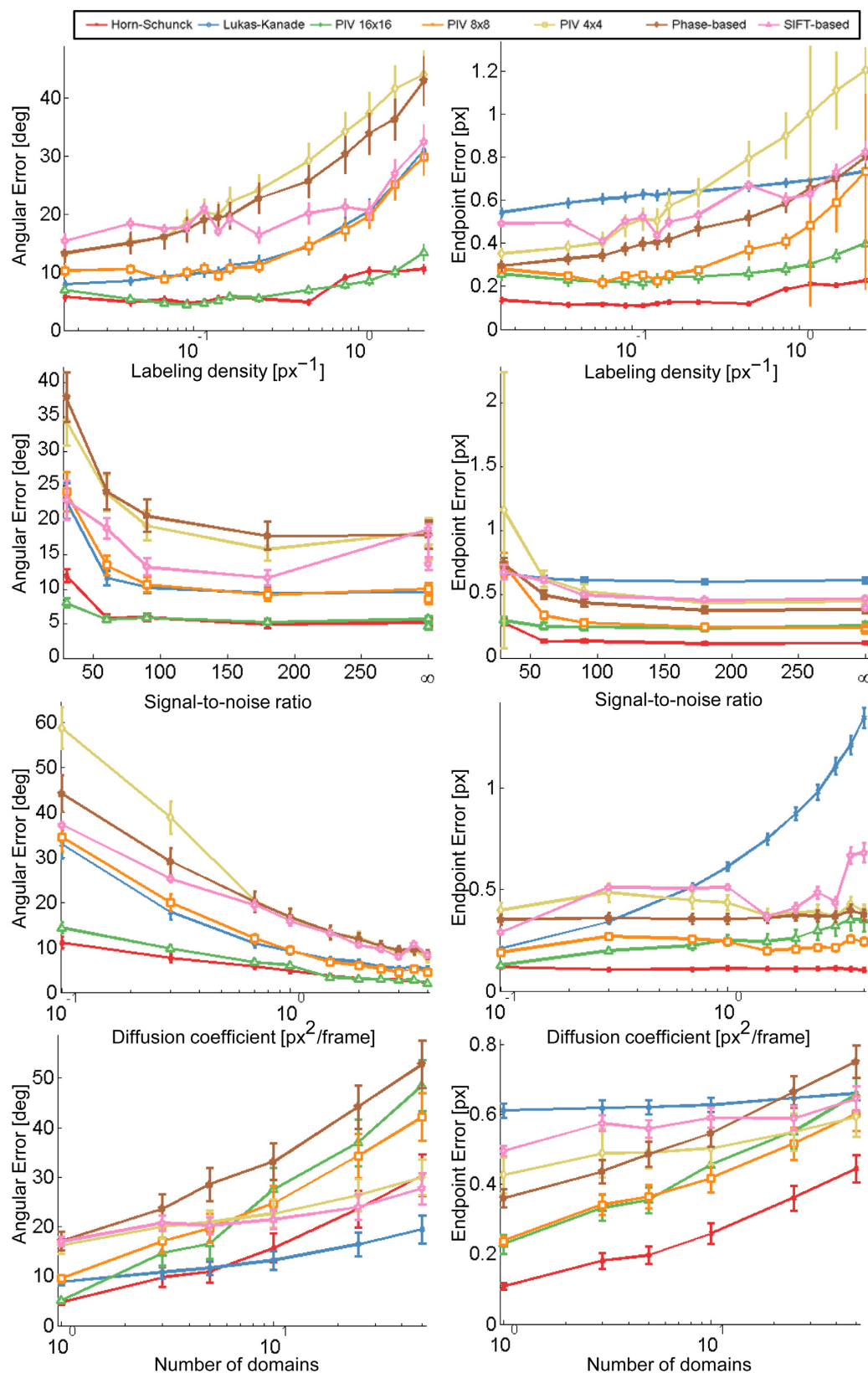


Figure 1. Performance of different OF methods. Angular and EE for each method is shown under variation of static (labeling density and SNR) and dynamic parameters (diffusion coefficient and number of domains). AE is shown in the left column, EE in the right; parameters are shown in rows and vary from low to high values. The response of each method in terms of AE and EE is plotted (see Supplementary Table 2 and Note 1). Error bars are symmetric and correspond to the standard deviation from 10 simulations. Lower AE and EE mean more accurate estimates.

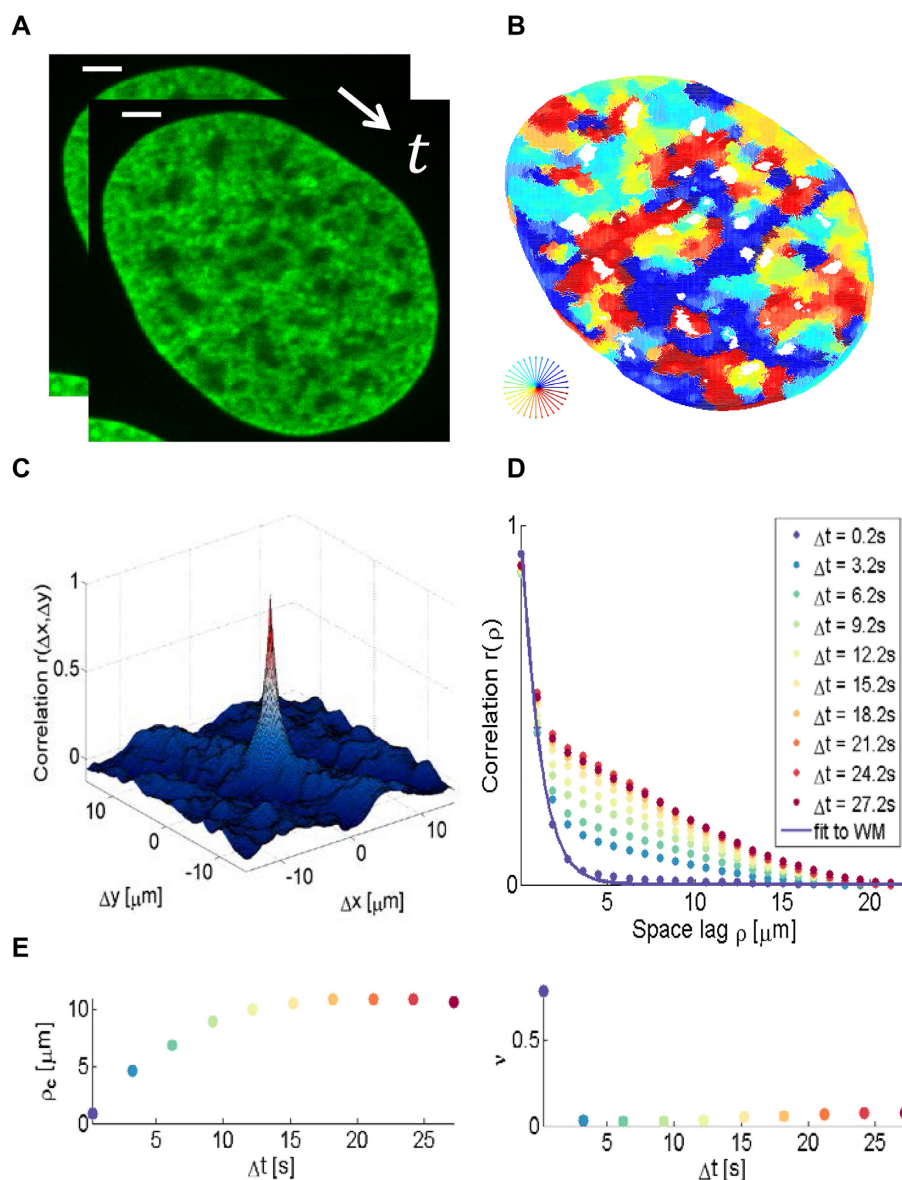


Figure 2. Schematic representation of the correlation analysis. (A) Two microscopy images (U2OS cells expressing H2B-GFP) were acquired with temporal resolution 200 ms. Scale bar is 3 μm . (B) The flow field between the input images was estimated by the Horn–Schunck formulation and color-coded as indicated in the lower right. Pixels in nucleoli appear empty due to the lack of intensity information. (C) Correlation calculation in two dimensions. (D) Empirical correlation (example shown for direction) was calculated as a function of space lag and fitted to the WM correlation model. Flow fields were estimated at every accessible time lags within the image series and each of them was fitted (example time lags shown only). (E) Correlation length ρ_c and the smoothness parameter ν were derived from the regression and shown over the time lag. The parameters were averaged for each time interval over all accessible time points. Note that with increasing time interval, less time points are available and therefore, the standard deviation (not shown) increases.

direction and magnitude. The fact that small regions arose by using the 16×16 pixel window size may be due to several independent motion areas within the interrogation window. Shifting the window from one pixel to another and including intensity information further apart from the vector to be estimated may therefore substantially influence vector estimation, even for adjacent pixels. In other words, averaging a vector over more than a micrometer for chromatin structures introduced errors in both direction and magnitude of the detected motion. Therefore, this approach led to inaccurate estimation of motion and correlation when simulating a high number of independently moving areas. The SIFT

method showed great similarity in correlation of direction and magnitude, which is likely due to vector quantization (integer values for the x and y-components of the flow vector are allowed only, see Supplementary Note 2). Only the HS-based method was able to identify changes in correlation over several space lags, and to distinguish between direction and magnitude.

Finally, the WM model enabled quantification of the correlation length as well as the smoothness parameter. The significance of the quantification of these parameters is illustrated in (Supplementary Note 2 and Supplementary Figure S3), where the response of parameter estimation is

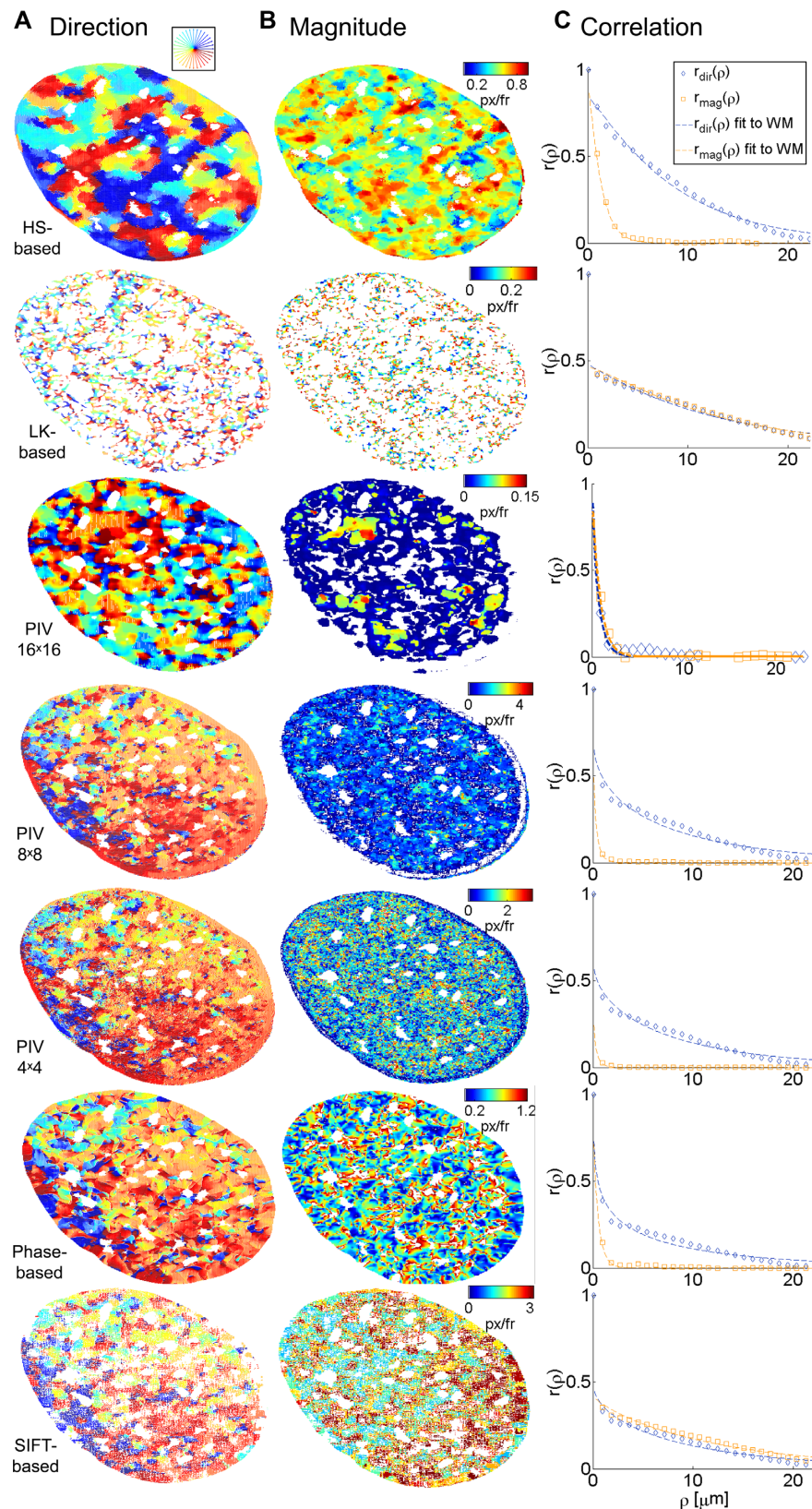


Figure 3. Visualization of flow fields for the analysis of a single U2OS cell expressing H2B-GFP. Rows correspond to the different investigated methods. Representative fields are shown. **(A)** Flow fields are color-coded by the direction of displacement vectors. **(B)** Magnitude of the corresponding flow vector color-coded from low to high as indicated by color bars. **(C)** Empirical correlation for direction (blue) and magnitude (orange) and corresponding fits to the WM model (solid lines) over space lags.

evaluated for several simulated scenarios of arising flow fields.

Chromatin dynamics at nano-scale resolution reveals transcription dependent long range correlation

We applied DFCC to analyze movements of chromatin in the entire nucleus and to assess whether chromatin dynamics were sensitive to transcriptional mode. Correlation of coherent chromatin motion was calculated using two different fluorescent labels: DNA labeled SiR–Hoechst and H2B fused to GFP in human osteosarcoma U2OS cells. Images were recorded in cells grown in medium containing serum (actively transcribing mode) and in cells starved in serum for 24 h (inactive mode). Analysis of chromatin motion in cells grown in medium containing serum showed that the correlation length for both DNA and H2B was time dependent, reaching a maximum correlation length ($\rho_c \approx 11 \mu\text{m}$) at 18.2 s (Figures 4C–D and 5C–D). Correlation over long range is consistent with the notion that active transcription occurs in numerous regions of decompacted, open chromatin (46). Interestingly, some regions of coherent motion comprise smaller areas of the scale of a few hundred nanometers within them, whose patterns deviate slightly from the direction of the bulk of the coherent domains (enlarged areas, Figures 4b and 5b) suggesting that all chromatin within territories of a single chromosome is not necessarily moving in the same direction or manner. This result concurs with previous observations that coherent regions of H2B-GFP movement spanned across several dNTP labeled CTs (6). Furthermore, flow fields comprised distinct regions of vortex-like motion of a few hundred nanometers length scale in all nuclei analyzed (Supplementary Figure S4a and b). Hence, the resolution achieved by our approach permits analysis of sub-micron motion within domains which may represent hubs of active DNA-associated processes, reminiscent of transcription and replication factories or sites of active long-range looping afforded by enhancers or replicon folding (12,22,47–49).

Quantification of spatial smoothness over large time intervals points to clear-cut boundaries between distinct regions, while smooth transitions in small neighborhoods dominate for short time intervals. These smooth transitions between regions of distinct motion indicate directed squeezing or stretching of chromatin boundaries suggestive of changes in local concentrations of actors regulating gene expression (Figure 6A and Supplementary Figure S4c).

In contrast, chromatin motion occurred in numerous small domains with smooth transitions in serum starved cells over 30 s (Figure 4C and D). The spatial correlation (both direction and magnitude) of SiR-labeled DNA showed almost no time dependence and fitting by the WM model yielded a correlation length of less than one micrometer (Figure 4C and D). The nearly constant spatial correlation is likely due to the fact that serum-starved cells are in quiescence, in which chromatin fibers are more compact (46,50). In conclusion, short correlation length and comparably high smoothness of flow may be due to condensed chromatin regions (Figure 6C and Supplementary Figure S4d).

However, motion of H2B-GFP in starved cells yielded a maximum directional correlation length of $\rho_c \approx 7 \mu\text{m}$, half the length calculated in cells with serum stimulation (Figure 5C and D), but greater than for motion of SiR-labeled DNA. Differences in the amplitude of correlation between SiR-labeled DNA and H2B-GFP might be due to variations in the labeling density affecting determination of domains and consequently correlation length calculations. Indeed, only 10–20% of chromatin contains labeled H2B-GFP (51) and this fraction may represent the least compacted fraction of total chromatin characterized by greater correlation length and roughness of flow. The residual correlation in serum starved cells could also stem from free H2B-GFP molecules not incorporated into chromatin.

Coordinated movements within domains correlate with RNA polymerase II activity

We further assessed the effect of transcription inhibitors on initiation or elongation of transcription by pre-treating the cells with DRB and TPL, respectively. Inhibition of RNA polymerase II (RNA pol II) had greater and more diverse effects when imaging SiR-labeled DNA than H2B-GFP (Figure 4C and D). Correlation length and magnitude of DNA motion was reduced in cells treated with DRB and only slightly affected by TPL compared to cells grown in serum, suggesting that elongation maintains dynamic transitions (Figure 4C and D). The relative smoothness of motion, however, remained similar to the one determined when cells were grown in serum, demonstrating that rough boundaries correspond to the presence of RNA pol II and cofactors in certain domains of the nucleus. Correlation length and relative smoothness of the motion of H2B-GFP upon RNA pol II inhibition were indistinguishable from the values determined in serum starved cells reinforcing the idea that active transcription drives H2B-GFP nuclear domain formation (Figure 5C and D). The magnitude of correlation increased at longer time intervals in inhibitor-treated nuclei but did not reach values determined in serum starved conditions. Hence, the remaining association of polymerases and cofactors during initiation (DRB causes RNA pol II to detach within the first exon (52)) or remaining elongation (TPL precludes RNA pol II from binding to the promoter but RNA pol II still elongating after 15 min treatment will proceed (53)) and possibly the presence of nascent mRNA influences dynamic behavior of chromatin.

The clear difference of coordinated movements between labeled DNA and H2B-GFP may also be exacerbated by loss of histones resulting from starvation- or inhibitor- induced stress (54). Histone levels varied slightly between the different conditions (Supplementary Figure S5). Our results showed similarities between actively transcribed (+serum) and initiation halted chromatin, where long scale correlation was seemingly due to chromatin compaction. Given that neither TPL nor DRB block RNA polymerase activity completely within the 15 min of our experiment, these observations strongly suggest that pausing transcription at an early stage does not abolish loop formation or long range contacts and coordinated motion of RNA pol II bound chromatin domains.

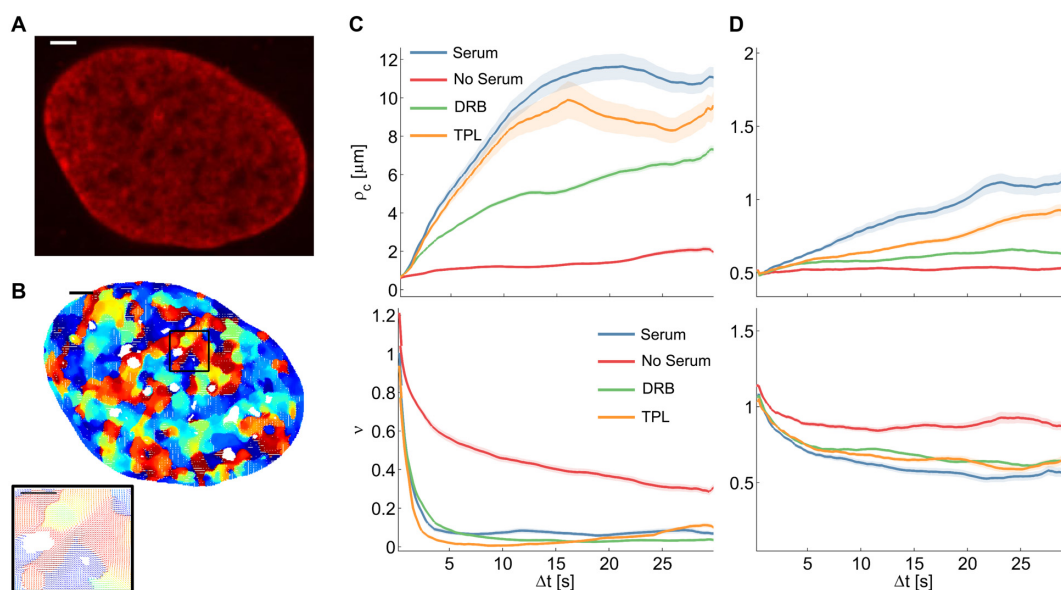


Figure 4. Correlation length and smoothness in direction and magnitude of DNA in U2OS cells using the WM model. (A) A fluorescence microscopy image of a nucleus where DNA was labeled using Sir-Hoechst; scale bar is 3 μm . (B) Flow field for $\Delta t = 0.2$ s and enlarged region (right) of the black rectangle; the field is color-coded according to the direction of the displacement. Scale bar is 3 μm (left) and 1 μm (right). (C) Correlation length (top) and smoothness parameter (bottom) calculated from regression of empirical correlation functions over time for directional correlation of flow fields. Different colors correspond to different conditions. Shaded error bars correspond to the standard deviation over 18 nuclei per condition. (D) As (C) for the vectors' magnitude.

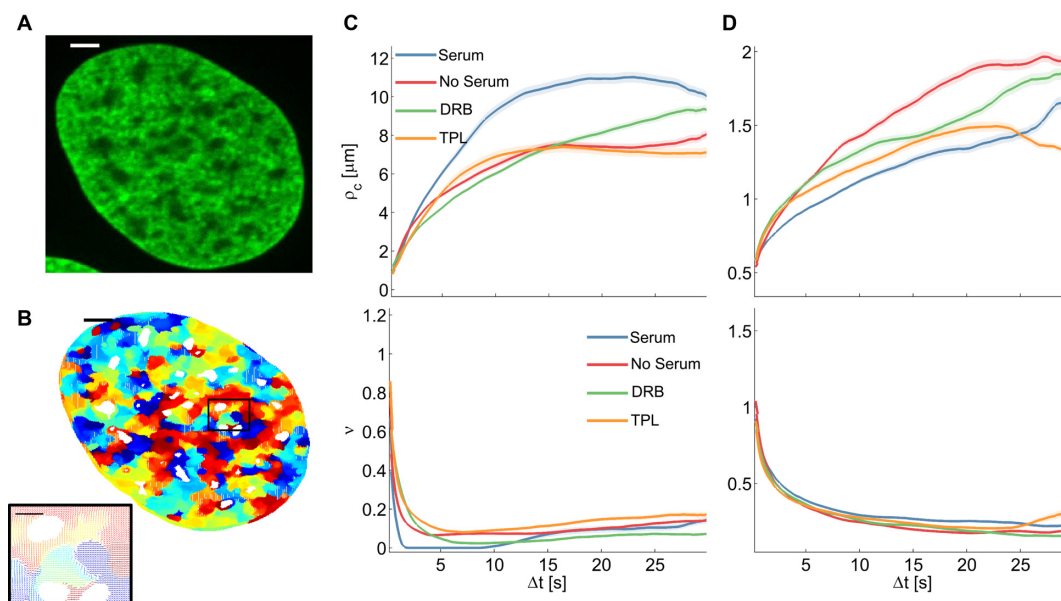


Figure 5. Correlation length and smoothness in direction and magnitude of H2B-tagged GFP in U2OS cells using the WM model. (A) A fluorescence microscopy image of a nucleus expressing H2B-GFP; scale bar is 3 μm . (B) Flow field for $\Delta t = 0.2$ s and zoomed-in region (right) of the black rectangle; the field is color-coded according to the direction of the displacement. Scale bar is 3 μm (left) and 1 μm (right). (C) Correlation length (top) and smoothness parameter (bottom) calculated from regression of empirical correlation functions over time lag for directional correlation of flow fields. Different colors correspond to different conditions. Shaded error bars correspond to the standard deviation over 19 nuclei per condition. (D) As (C) for the vectors' magnitude.

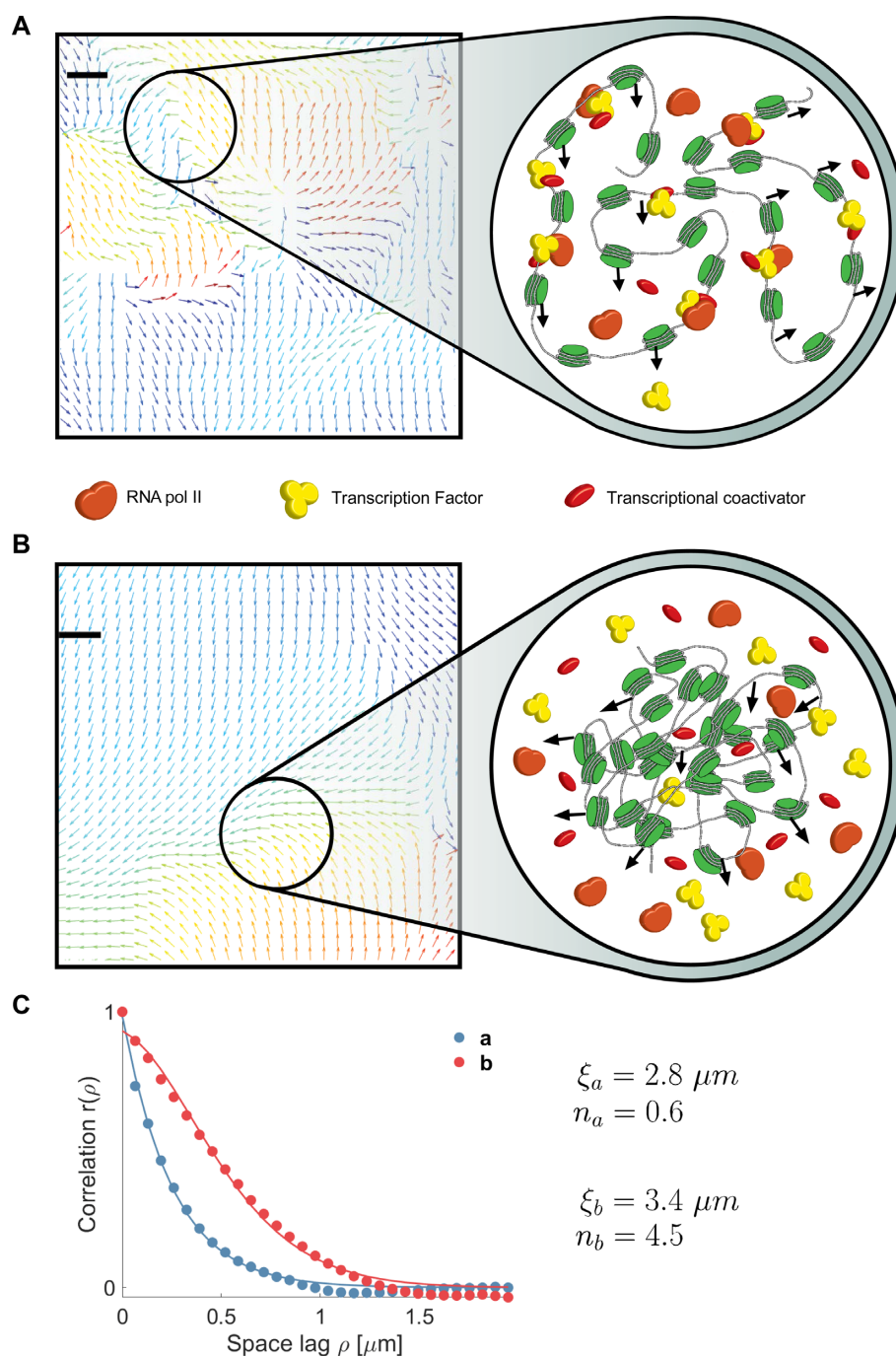


Figure 6. Representative magnification of flow fields illustrating flow smoothness and models of proposed mechanisms. The observed change in smoothness between serum stimulation (**A**) and starvation (**B**) in case of DNA probing is visualized by representative regions (Supplementary Figure S4). The observed low smoothness after serum stimulation may reflect chromatin decompaction. Chromatin is able to move rather freely and RNA pol II and transcription factors can bind to DNA. Coherent motion and sharp motion boundaries were observed and suggestive of defined DNA-processing hubs or factories. In case of serum starvation, correlation drops and coherently moving regions seamlessly interrelate. An increase in chromatin compaction causes DNA–DNA interactions to occur more frequently resulting in smooth spatial transitions between directional chromatin motion. Scale bars are 200 nm. (**C**) Correlation functions for the flow fields shown in panel (A) and (B) are fit to the WM model.

CONCLUSION

By using OF, we detected coordinated domains of chromatin motion in living human cells with nano-scale sensitivity. Chromatin domains of coherent motion exhibit long range correlation over the entire nucleus. In the absence of transcriptional activity, chromatin movements were no longer correlated and exhibited constant, but small correlation lengths. Because protein and mRNA concentration as well as transient contacts and looping change during transcription, they also affect the mechanical properties of the chromatin fiber (22,56).

Notably, correlation length based on direction and magnitude of DNA significantly differed from H2B-GFP. Despite absence of apparent defects in cell proliferation, we cannot exclude that the SiR Hoechst dye alters chromatin diffusive behavior, nor can we ascertain that the extra bulk imposed on the nucleosomes by incorporating H2B fused to GFP (a 12 or 25% increase in molecular weight of the octamer for homo- and heterotypic nucleosomes, respectively) affects the analysis. Although no noticeable consequences, if any, of this extra bulk, were reported in previous studies (6,26,27). We could, however, explain the differences in our results by a difference in labeling density and preferential incorporation of H2B-GFP into more open region of chromatin. Hence, analyzing DNA provides a more general, possibly more precise, picture with greater amplitudes between different chromatin states including inactive, dense chromatin domains, where H2B-GFP mostly informs on the behavior of more accessible chromatin.

We further show that transcription-dependent motion is characterized by the appearance of vortex-like movements which are suggestive of nodes. Nodes are formed by accumulation of proteins and enzymes involved in a specific process, for example polycomb or chromatin remodelers regulating transcription (56–59). One could speculate that vortex-like apparent motion at short time scales may result from active DNA pulling or long-range looping afforded by enhancers or from folding of replicons at specific sites or within transcription or replication factories (12,22,47–49).

The smoothness parameter allows quantification of transitions in motion and provides insight into the origin of chromatin domains. Smoothness values are characteristic of transcription induced variations in chromatin compactness. The smoothness parameter can be interpreted as a measure of smooth or sharp transitions between adjacent regions of coherent flow and therefore provides insight into time dependent formation of dynamic regions and their boundaries.

Chromatin conformation capture analysis have identified A and B compartments regrouping <10 Mb domains of similar chromatin marks and compaction (3,60). Blocks of several A or B compartments tend to interact but their assembly is stochastic and their boundaries cannot be assessed by population averaging Hi-C methods. Domains likely result from auto-assembly (61) or phase separation-type physical processes driven by accumulation of proteins (62), such as for example RNA pol II hubs (12), HP1 droplets (63) or repeated elements (64). On the single cell level, sharp boundaries of compartments were also seen in snapshots using super-resolution microscopy (65). Hence,

the rough domain boundaries observed in this study are reminiscent of phase transitions, as they separate domains of different dynamic behavior depending on transcriptional activity. Our approach allows seeing functional domains in nuclei of living cells in real time.

DATA AVAILABILITY

The code of for the DFCC approach is available in MATLAB which can be downloaded from this link (<https://github.com/romanbarth/DFCC>). Data are available on request.

SUPPLEMENTARY DATA

Supplementary Data are available at NAR Online.

ACKNOWLEDGEMENTS

We thank Sébastien Huet (IGDR-UMR6290, Rennes, France) for providing the U2OS H2B-GFP cell line. Alain Kamgoue helped with setting up the Amazon EC2 computation cluster that was used for our calculations. We acknowledge support from the TRI imaging platform, Toulouse.

FUNDING

ANR ANDY; IDEX ATs NudGENE; Foundation ARC; INSERM; Cancer and Epigenetics; Centre National de la Recherche Scientifique [PLBIO2016]. Funding for open access charge: INSERM; Epigenetics and Cancer.

Conflict of interest statement. None declared.

REFERENCES

- Cremer, T., Kurz, A., Zirbel, R., Dietzel, S., Rinke, B., Schrock, E., Speicher, M.R., Mathieu, U., Jauch, A., Emmerich, P. *et al.* (1993) Role of chromosome territories in the functional compartmentalization of the cell nucleus. In: *Cold Spring Harbor Symposia on Quantitative Biology*. Cold Spring Harbor Laboratory Press, NY, Vol. 58, pp. 777–792.
- Bolzer, A., Kreth, G., Solovei, I., Koehler, D., Saracoglu, K., Fauth, C., Müller, S., Eils, R., Cremer, C., Speicher, M.R. *et al.* (2005) Three-dimensional maps of all chromosomes in human male fibroblast nuclei and prometaphase rosettes. *PLoS Biol.*, 3, 826–842.
- Lieberman-Aiden, E., Van Berkum, N.L., Williams, L., Imakaev, M., Ragoczy, T., Telling, A., Amit, I., Lajoie, B.R., Sabo, P.J., Dorschner, M.O. *et al.* (2009) Comprehensive mapping of Long-Range interactions reveals folding principles of the human genome. *Science*, 326, 289–293.
- Bornfleth, H., Edelmann, P., Zink, D., Cremer, T. and Cremer, C. (1999) Quantitative motion analysis of subchromosomal foci in living cells using four-dimensional microscopy. *Biophys. J.*, 77, 2871–2886.
- Maeshima, K., Hihara, S. and Eltsov, M. (2010) Chromatin structure: does the 30-nm fibre exist in vivo? *Curr. Opin. Cell Biol.*, 22, 291–297.
- Zidovska, A., Weitz, D.A. and Mitchison, T.J. (2013) Micron-scale coherence in interphase chromatin dynamics. *Proc. Natl. Acad. Sci. U.S.A.*, 110, 15555–15560.
- Henikoff, S. (2016) Mechanisms of nucleosome dynamics in vivo. *Cold Spring Harb. Perspect. Med.*, 6, 1–15.
- Marnef, A. and Legube, G. (2017) Organizing DNA repair in the nucleus: DSBs hit the road. *Curr. Opin. Cell Biol.*, 46, 1–8.
- Voss, T.C. and Hager, G.L. (2013) Dynamic regulation of transcriptional states by chromatin and transcription factors. *Nat. Rev. Genet.*, 15, 69–81.

10. Carter,D., Chakalova,L., Osborne,C.S., Dai,Y. and Fraser,P. (2002) Long-range chromatin regulatory interactions in vivo. *Nat. Genet.*, **32**, 623–626.
11. Osborne,C.S., Chakalova,L., Brown,K.E., Carter,D., Horton,A., Debrand,E., Goyenechea,B., Mitchell,J.A., Lopes,S., Reik,W. *et al.* (2004) Active genes dynamically colocalize to shared sites of ongoing transcription. *Nat. Genet.*, **36**, 1065–1071.
12. Feuerborn,A. and Cook,P.R. (2015) Why the activity of a gene depends on its neighbors. *Trends Genet.*, **31**, 483–490.
13. Cremer,T. and Cremer,C. (2001) Chromosome territories, nuclear architecture and gene regulation in mammalian cells. *Nat. Rev. Genet.*, **2**, 292–301.
14. Verschure,P.J., Van Der Kraan,I., Manders,E.M.M. and Van Driel,R. (1999) Spatial relationship between transcription sites and chromosome territories. *J. Cell Biol.*, **147**, 13–24.
15. Zirbel,R.M., Mathieu,U.R., Kurz,A., Cremer,T. and Lichter,P. (1993) Evidence for a nuclear compartment of transcription and splicing located at chromosome domain boundaries. *Chromosom. Res.*, **1**, 93–106.
16. Chambeyron,S. and Bickmore,W.A. (2004) Chromatin decondensation and nuclear reorganization of the HoxB locus upon induction of transcription. *Genes Dev.*, **18**, 1119–1130.
17. Belmont,A.S., Li,G., Sudlow,G. and Robinett,C. (1998) Chapter 13: visualization of Large-Scale chromatin structure and dynamics using the lac operator/lac repressor reporter system. *Methods Cell Biol.*, **58**, 203–222.
18. Heun,P. (2001) Chromosome dynamics in the yeast interphase nucleus. *Science*, **294**, 2181–2186.
19. Chubb,J.R., Boyle,S., Perry,P. and Bickmore,W.A. (2002) Chromatin motion is constrained by association with nuclear compartments in human cells. *Curr. Biol.*, **12**, 439–445.
20. Levi,V., Ruan,Q., Plutz,M., Belmont,A.S. and Gratton,E. (2005) Chromatin dynamics in interphase cells revealed by tracking in a Two-Photon excitation microscope. *Biophys. J.*, **89**, 4275–4285.
21. Chuang,C.H., Carpenter,A.E., Fuchsova,B., Johnson,T., de Lanerolle,P. and Belmont,A.S. (2006) Long-Range directional movement of an interphase chromosome site. *Curr. Biol.*, **16**, 825–831.
22. Germier,T., Kocanova,S., Walther,N., Bancaud,A., Shaban,H.A., Sellou,H., Politi,A.Z., Ellenberg,J., Gallardo,F. and Bystricky,K. (2017) Real-time imaging of a single gene reveals Transcription-Initiated local confinement. *Biophys. J.*, **113**, 1383–1394.
23. Jegou,T., Chung,I., Heuvelman,G., Wachsmuth,M., Görisch,S.M., Greulich-Bode,K.M., Boukamp,P., Lichter,P. and Rippe,K. (2009) Dynamics of telomeres and promyelocytic leukemia nuclear bodies in a Telomerase-negative human cell line. *Mol. Biol. Cell*, **20**, 2070–2082.
24. Molenaar,C., Wiesmeijer,K., Verwoerd,N.P., Khazen,S., Eils,R., Tanke,H.J. and Dirks,R.W. (2003) Visualizing telomere dynamics in living mammalian cells using PNA probes. *EMBO J.*, **22**, 6631–6641.
25. Chen,B., Gilbert,L.A., Cimini,B.A., Schnitzbauer,J., Zhang,W., Li,G.-W., Park,J., Blackburn,E.H., Weissman,J.S., Qi,L.S. *et al.* (2013) Dynamic imaging of genomic loci in living human cells by an optimized CRISPR/Cas system. *Cell*, **155**, 1479–1491.
26. Shinkai,S., Nozaki,T., Maeshima,K. and Togashi,Y. (2016) Dynamic nucleosome movement provides structural information of topological chromatin domains in living human cells. *PLoS Comput. Biol.*, **12**, e1005136.
27. Nozaki,T., Imai,R., Tanbo,M., Nagashima,R., Tamura,S. and Tani,T. (2017) Dynamic organization of chromatin domains revealed by super-resolution live-cell imaging. *Mol. Cell*, **10**, 1–12.
28. Vig,D.K., Hamby,A.E. and Wolgemuth,C.W. (2016) On the quantification of cellular velocity fields. *Biophys. J.*, **110**, 1469–1475.
29. Lukinavičius,G., Blaukopf,C., Pershagen,E., Schena,A., Derivery,E., Gonzalez-gaitan,M., Este,E.D., Hell,S.W., Gerlich,D.W. and Johnsson,K. (2015) A far-red DNA stain for live-cell nanoscopy. *Nat. Commun.*, **6**, 1–5.
30. Horn,B.K.P. and Schunck,B.G. (1981) Determining optical flow. *Artif. Intell.*, **17**, 185–203.
31. Lucas,B.D. and Kanade,T. (1981) An iterative image registration technique with an application to stereo vision. *Imaging*, **130**, 674–679.
32. Svein,J.K. (2004) An introduction to MatPIV v. 1.6.1. *Dep. Math. Univ. Oslo, Oslo, Norw.*, 1–27.
33. Gautama,T. and Van Hulle,M.A. (2002) A phase-based approach to the estimation of the optical flow field using spatial filtering. *IEEE Trans. Neural Networks*, **13**, 1127–1136.
34. Liu,C., Yuen,J. and Torralba,A. (2011) Sift flow: Dense correspondence across scenes and its applications. In: *IEEE Transactions on Pattern Analysis and Machine Intelligence*. Vol. **33**, pp. 978–994.
35. Fleet,D.J. and Jepson,A.D. (1990) Computation of component image velocity from local phase information. *Int. J. Comput. Vis.*, **5**, 77–104.
36. Otte,M. and Nagel,H.-H. (1994) Optical flow estimation: advances and comparisons. *Comput. Vision-ECCV'94*, 49–60.
37. Tomasi,C. and Manduchi,R. (1998) Bilateral filtering for gray and color images. *Proc. 1998 IEEE Int. Conf. Comput. Vis.*, doi:10.1109/ICCV.1998.710815.
38. Petersen,N.O., Höddelius,P.L., Wiseman,P.W., Seger,O. and Magnusson,K.E. (1993) Quantitation of membrane receptor distributions by image correlation spectroscopy: concept and application. *Biophys. J.*, **65**, 1135–1146.
39. Mateérn,B. (1986) *Spatial variation*. Springer, NY.
40. Gneiting,T., Kleiber,W. and Schlather,M. (2010) Matérn Cross-covariance functions for multivariate random fields. *J. Am. Stat. Assoc.*, **105**, 1167–1177.
41. Stein,M.L. (1999) *Interpolation of Spatial Data: Some Theory for Kriging*. Springer, NY.
42. Stoyan,D. (2007) Matérn, B.: *Spatial Variation*. 2nd Ed., Springer-Verlag, Berlin, Heidelberg, New York, London, Paris, Tokyo 1986, 151 S., DM 33,-. *Biometrical J.*, **30**, 594–594.
43. Guttorp,P. and Gneiting,T. (2005) On the Whittle-Matérn correlation family. *NRCSE-TRS, University of Washington*, **80**, <http://www.nrcse.washington.edu/pdf/trs81.pdf>.
44. Westerweel,J. (1997) Digital particle image velocimetry. *Meas. Sci. Technol.*, **8**, 1379–1392.
45. Levi,V., Ruan,Q., Plutz,M., Belmont,A.S. and Gratton,E. (2005) Chromatin dynamics in interphase cells revealed by tracking in a two-photon excitation microscope. *Biophys. J.*, **89**, 4275–4285.
46. Wang,Y., Maharana,S., Wang,M.D. and Shivashankar,G.V. (2015) Super-resolution microscopy reveals decondensed chromatin structure at transcription sites. *Sci. Rep.*, **4**, 4477.
47. Hozák,P., Hassan,A.B., Jackson,D.A. and Cook,P.R. (1993) Visualization of replication factories attached to a nucleoskeleton. *Cell*, **73**, 361–373.
48. Chagin,V.O., Casas-Delucchi,C.S., Reinhart,M., Schermelleh,L., Markaki,Y., Maiser,A., Bolius,J.J., Bensimon,A., Fillies,M., Domaing,P. *et al.* (2016) 4D Visualization of replication foci in mammalian cells corresponding to individual replicons. *Nat. Commun.*, **7**, 11231.
49. Stavreva,D.A. and Hager,G.L. (2016) Chromatin structure and gene regulation: a dynamic view of enhancer function. *Nucleus*, **20**, 1–7.
50. Xiao,G.-H. (2001) Anti-apoptotic signaling by hepatocyte growth factor/Met via the phosphatidylinositol 3-kinase/Akt and mitogen-activated protein kinase pathways. *Proc. Natl. Acad. Sci. U.S.A.*, **98**, 247–252.
51. Sellou,H., Lebeaupin,T., Chapuis,C., Smith,R., Hegele,A., Singh,H.R., Kozłowski,M., Bultmann,S., Ladurner,A.G., Timinszky,G. *et al.* (2016) The poly(ADP-ribose)-dependent chromatin remodeler Alc1 induces local chromatin relaxation upon DNA damage. *Mol. Biol. Cell*, **27**, 3791–3799.
52. Wijgerde,M., Grosveld,F. and Fraser,P. (1995) Transcription complex stability and chromatin dynamics in vivo. *Nature*, **377**, 209–213.
53. Saunders,A., Core,L.J. and Lis,J.T. (2006) Breaking barriers to transcription elongation. *Nat. Rev. Mol. Cell Biol.*, **7**, 557–567.
54. Hauer,M.H., Seeber,A., Singh,V., Thierry,R., Sack,R., Amitai,A., Kryzhanovska,M., Eglinger,J., Holcman,D., Owen-Hughes,T. *et al.* (2017) Histone degradation in response to DNA damage enhances chromatin dynamics and recombination rates. *Nat. Struct. Mol. Biol.*, **24**, 99–107.
55. Schoenfelder,S., Sugar,R., Dimond,A., Javierre,B.-M., Armstrong,H., Mifsud,B., Dimitrova,E., Matheson,L., Tavares-Cadete,F., Furlan-Magaril,M. *et al.* (2015) Polycomb repressive complex PRC1 spatially constrains the mouse embryonic stem cell genome. *Nat. Genet.*, **47**, 1179–1186.
56. Jin,F., Li,Y., Dixon,J.R., Selvaraj,S., Ye,Z., Lee,A.Y., Yen,C.-A., Schmitt,A.D., Espinoza,C.A. and Ren,B. (2013) A high-resolution

- map of the three-dimensional chromatin interactome in human cells. *Nature*, **503**, 290–294.
58. Pancaldi, V., Carrillo-de-Santa-Pau, E., Javierre, B.M., Juan, D., Fraser, P., Spivakov, M., Valencia, A. and Rico, D. (2016) Integrating epigenomic data and 3D genomic structure with a new measure of chromatin assortativity. *Genome Biol.*, **17**, 152.
 59. Simonis, M., Klous, P., Splinter, E., Moshkin, Y., Willemsen, R., de Wit, E., van Steensel, B. and de Laat, W. (2006) Nuclear organization of active and inactive chromatin domains uncovered by chromosome conformation capture-on-chip (4C). *Nat. Genet.*, **38**, 1348–1354.
 60. Sexton, T., Yaffe, E., Kenigsberg, E., Bantignies, F., Leblanc, B., Hoichman, M., Parrinello, H., Tanay, A. and Cavalli, G. (2012) Three-dimensional folding and functional organization principles of the *Drosophila* genome. *Cell*, **148**, 458–472.
 61. Misteli, T. (2007) Beyond the sequence: cellular organization of genome function. *Cell*, **128**, 787–800.
 62. Hnisz, D., Shrinivas, K., Young, R.A., Chakraborty, A.K. and Sharp, P.A. (2017) A phase separation model for transcriptional control. *Cell*, **169**, 13–23.
 63. Tatarakis, A., Behrouzi, R. and Moazed, D. (2017) Evolving models of Heterochromatin: from foci to liquid droplets. *Mol. Cell*, **67**, 725–727.
 64. Tang, S.J. (2017) Potential role of phase separation of repetitive DNA in chromosomal organization. *Genes*, **8**, 279.
 65. Cremer, T. and Cremer, C. (2001) Chromosome territories, nuclear architecture and gene regulation in mammalian cells. *Nature Reviews Genetics*, **2**, 292–301.